HOKKAIDO UNIVERSITY

Title	The effect of anodizing temperature on the oxygen evolution reaction activity of anodized FeNiCo alloy in alkaline electrolyte
Author(s)	Nishimoto, Masahiro; Xiong, Zetao; Kitano, Sho; Aoki, Yoshitaka; Habazaki, Hiroki
Citation	Electrochimica acta, 427, 140875 https://doi.org/10.1016/j.electacta.2022.140875
Issue Date	2022-09-20
Doc URL	http://hdl.handle.net/2115/92804
Rights	© 2022. This manuscript version is made available under the CC-BY-NC-ND 4.0 license http://creativecommons.org/licenses/by-nc-nd/4.0/
Rights(URL)	http://creativecommons.org/licenses/by-nc-nd/4.0/
Type	article (author version)
File Information	FeNiCo_temp_rev2c.pdf

Instructions for use

Hokkaido University Collection of Scholarly and Academic Papers : HUSCAP

The effect of anodizing temperature on the oxygen evolution reaction activity of anodized FeNiCo alloy in alkaline electrolyte

Masahiro Nishimoto[a], Zetao Xiong[a], Sho Kitano[b], Yoshitaka Aoki[b], Hiroki Habazaki[b,*]

[a] Graduate School of Chemical Sciences and Engineering, Hokkaido University, Sapporo, Hokkaido 060-8628, Japan

[b] Division of Applied Chemistry, Faculty of Engineering, Hokkaido University, Sapporo, Hokkaido 060-8728, Japan

*Corresponding author: habazaki@eng.hokudai.ac.jp

Abstract

This study investigates the oxygen evolution reaction (OER) activity of the FeNiCo alloy anodized at several temperatures in a fluoride-containing ethylene glycol electrolyte. When the alloy is anodized at 10 V, the OER activity in KOH electrolyte is highly enhanced on the alloy anodized at 15 and 20°C, at which non-uniform film growth proceeds. The fraction of the locally thick film regions increases with anodizing time, enhancing the OER activity. Only thin porous films are formed at ≥30°C even though the anodizing current is high because of the promotion of film dissolution at high electrolyte temperatures. Because of the thickness limitation, the OER activity is relatively low when the anodic films are formed at ≥30°C. A good correlation is found between the OER activity and the electric double-layer capacitance; thicker porous anodic films enhance the OER activity. The anodic film formed at each temperature consists of a rutile-type (FeNiCo)F_2 phase, but in KOH electrolyte, it is converted readily to an oxyhydroxide phase, which is OER active. A ~2 μm-thick film obtained under the optimum anodizing condition reduces the overpotential of OER to 245 mV at 10 mA cm^{-2} in 0.1 mol dm^{-3} KOH electrolyte.

Keywords: anodizing, oxygen evolution reaction, oxyhydroxide, FeNiCo, electrocatalyst

1. Introduction

Hydrogen production from renewable sources, including the sun, wind, and hydropower, is vital to reducing carbon dioxide emissions to the air from fossil fuel combustion. Hydrogen gas can be produced by alkaline water splitting, polymer electrolyte membrane electrolysis, and solid oxide electrolysis, of which alkaline water splitting is the most cost-effective and noble metals are not required as electrocatalysts [1, 2]. To produce hydrogen more efficiently, however, the high overpotential of oxygen evolution reaction (OER) needs to be lowered.

The iron-doped nickel hydroxides and oxyhydroxides have received increased attention as highly active OER electrocatalysts in alkaline environments [3-11]. Trotochaud et al. reported the marked reduction of OER overpotential by iron inclusion in NiOOH and discussed the enhancing mechanism [6]. They found that the film conductivity of β-NiOOH increased with iron addition by 30 times, but the activity enhancement was not fully explained by the increase in conductivity. They proposed a partial charge-transfer activation effect of iron. Similarly, the same group reported enhancement of OER activity on CoOOH by adding iron [13]. They suggested that iron is the most active catalyst site, even though the activation mechanism still needs to be figured out. Zhu et al. reported that Fe^{3+} ions were incorporated into β-$Ni(OH)_2$, with the OER activity enhancing as Fe^{3+} content increases. The $(Ni_{0.5}Fe_{0.5})(OH)_2$ showed the very low overpotential of 0.26 V at 10 mA cm^{-2} in 1 mol dm^{-3} KOH electrolyte. It was also discussed that the structural transformation by iron addition contributed to the OER activity enhancement. The iron incorporation often developed a layered double hydroxide (LDH) phase, and the iron-containing LDHs were active for OER [12].

These OER active iron-containing nickel or cobalt (oxy)hydroxides have been prepared usually as powders or nanosheets. These electrocatalysts need to be loaded on a metallic

current collector with an organic binder and often a conductive additive to prepare practical OER electrodes. However, the binder often covers the electrocatalytic active sites, and detachment of electrocatalysts likely occurs due to vigorous gas evolution in operation [13].

Recently, an anodizing process has received increasing attention in fabricating OER-active electrodes. Nanoporous and nanotubular anodic films with high surface areas can be developed readily by anodizing metals and alloys. Such anodic films adherent to the substrate were also formed on iron [14-17], cobalt [18], and nickel substrates [19-21]. It was recently reported that anodizing of nickel form enhanced OER activity, particularly in an unpurified alkaline electrolyte, in which iron impurity in the electrolyte was incorporated in the porous layer [22]. Schäfer et al. reported the increased OER activity of the commercial Ni42 steel by anodizing [23], and Fan et al. demonstrated the overpotential as low as 0.17 V by anodizing of FeCoNi alloy [24]. Concerning the activation of OER by anodizing, it was reported that the formation of defect-enriched oxyfluoride was important in OER activity [25]. However, quite recently, Yamada et al. reported that the porous oxyfluoride film formed by anodizing NiFe alloys was converted to hydroxide during potential cycling in KOH electrolyte, during which the OER activity was highly increased [26]. When the FeNiCo alloy anodized in the fluoride-containing organic electrolyte was used for OER in KOH electrolyte, high OER activity was immediately obtained due to the rapid conversion of oxyfluoride to an OER active amorphous oxyhydroxide [27]. Accordingly, simple anodizing of metals is an interesting and practical activation method to develop highly active OER electrodes.

For the activation of alloy electrodes by anodizing, the anodizing conditions may influence the activity because of the change in film morphology, thickness, and composition. Thus, in this study, porous anodic films were formed on the commercial FeNiCo alloy under various temperatures in fluoride-containing organic electrolyte. Their OER activities were examined to elucidate the optimum porous anodic films to get higher OER activity.

2. Experimental

This study used a FeNiCo alloy containing 29.72 wt % Ni and 16.28 wt % Co, obtained from Nilaco Corp., Japan. This alloy is usually referred to as Kovar alloy. The formation of nanoporous anodic films was conducted by anodizing the alloy at 10 V in 0.54 mol dm^{-3} NH_4F + 2.5 mol dm^{-3} H_2O/ethylene glycol electrolyte at temperatures from 10°C to 40°C using a two-electrode cell with a Pt counter electrode. Post-washing was performed in ethylene glycol to avoid the compositional change by washing in water, and then the anodized specimens were dried in the air at room temperature. EDS analysis confirmed the fluoride-rich composition of the anodic films.

To determine the OER activity in 1.0 mol dm^{-3} KOH electrolyte at room temperature, we used a potentiostat (Princeton Applied Research, Versastat4) equipped with a frequency response analyzer. With a three-electrode cell containing a Pt counter electrode and a Hg/HgO/1 mol dm^{-3} KOH reference electrode, the cyclic voltammetry (CV) was conducted by sweeping the potential at 10 mV s^{-1}. The conditions of the EIS measurements were as follows; a frequency range of 0.1 Hz - 100 kHz and an ac amplitude of 10 mV at 1.5 V vs RHE. The electric double-layer capacitance was also estimated from cyclic voltammetry at sweep rates of 10 -140 mV s^{-1} between 0.74 and 0.88 V versus RHE [28].

A field-emission scanning electron microscopy (FE-SEM; ZEISS, Sigma-500) was used to observe surfaces and cross-sections of electrodes. A broad ion beam cross-section polisher (JEOL, IB-19530CP) was used and operated at an argon ion energy of 8 kV to prepare cross-sections. Compositional analysis was performed using energy-dispersive X-ray spectroscopy (EDS; Brucker, Quantex) attached with FE-SEM. The electron beam accelerating voltage of 3 kV was used for the EDS analysis. Under this accelerating voltage, the analytical depth of the anodic films was less than 150 nm, which was thinner than the thickness of the anodic films,

and Lα lines of Fe, Ni, and Co were used for quantification. An X-ray diffraction analysis was performed under the α-2θ (α = 2°) mode with Cu Kα radiation (λ = 0.15418 nm) to identify the phases within the electrodes. Raman spectroscopy with a 532 nm laser beam (Horiba Scientific, XploRA) was also used to identify phases in the electrodes. X-ray photoelectron spectroscopy (XPS) analysis (JEOL, JSP-9200) was also conducted for the surface characterization of the anodized specimens after OER. The peak binding energy was calibrated using a contaminant hydrocarbon peak of 285.0 eV. The surface composition was estimated from the peak area of each element, which was determined using a JEOL, SpecSurf software.

3. Results and Discussion

Fig. 1a shows the current transients of the alloy during anodizing at 10 V in NH_4F + H_2O/ethylene glycol electrolyte at several temperatures for 30 min. The current decreases initially, showing a minimum before reaching the steady-state current at 30 and 40°C. Such current transient is typical in growing porous anodic films on aluminum in acid electrolytes [29]. The initial current reduction is related to thickening the barrier anodic oxide layer, and the following current increase occurs due to the pore initiation by local field-assisted dissolution [30]. Anodizing typically creates a thin barrier anodic oxide layer beneath the porous anodic layer. The thickness of the barrier anodic oxide layer, where a high electric field is applied during anodizing, should be constant at the steady-state current density. The current transient becomes more complex at lower temperatures, and the minimum current appears after a quasi-steady-state current. The complex current transient may be associated with the non-uniform film growth, which is discussed later, but the detailed understanding is a subject of future study. In addition, longer time needs to reach the steady-state current density at lower temperatures, and no steady-state appears within 30 min at 10°C. A decrease in the

anodizing temperature results in decline in steady-state current density. The steady-state current was maintained up to 2 h at 20°C, as shown in Fig. 1b.

We analyzed XRD patterns on the anodic films developed at various temperatures (Fig. 1c). Besides intense peaks from the alloy substrate with a face-centered cubic structure, weak peaks assigned to a rutile-type (FeCoNi)F_2 phase were observed at each temperature. The peak intensity of this phase is highest at 20°C, suggesting the formation of the thickest film. The reduction of the peak intensity at higher temperatures is associated with the inner film formation, as discussed later. The formation of the fluoride phase is consistent with the previous studies [26, 27].

By measuring the CV response of the anodized alloy specimens in 1.0 mol dm^{-3} KOH electrolyte at room temperature, the OER activity of the alloy electrodes was determined. Several CV cycles were conducted for each specimen, during which no significant change in the CV curves was found for both as-received and anodized alloy specimens. This is a characteristic feature of this alloy [27], whereas the OER current of the anodized Ni and Ni-rich Ni-Fe alloys was initially low and subsequently increased during CV cycles [26]. During CV cycles, the present anodized alloy exhibits stable OER activity due to rapid conversion of the fluoride phase [28]. All the anodized alloy electrodes show enhanced OER activity compared with the as-received alloy specimen; however, the OER activity is dependent on the anodizing temperature. The alloy anodized at 15 and 20°C exhibits the highest activity, showing a low overpotential of 0.248 V at 10 mA cm^{-2}. The OER activities of the alloy anodized at 30 and 40°C are similar. However, their overpotential of 0.29 V is higher than that of the alloy anodized at 15 and 20°C. It is evident from Fig. 2a that the overpotential of the alloy at the optimized temperature is also lower than that of the OER active RuO_2 electrocatalyst. The Tafel plots, shown in Fig. 2b, disclose a relatively small Tafel slope of 37-39 mV $decade^{-1}$ regardless of the anodizing temperature, and the value is smaller than that of

RuO_2 (64 mV decade^{-1}). The small Tafel slope is an advantage in reducing the overpotential at high current density, which is necessary for practical electrolysis for hydrogen production.

In addition, we examined the influence of anodizing time on the OER activity for the alloy anodized at 20°C. Fig. 2c illustrates the increased OER activity with anodizing time. The correlation between the OER overpotential and the anodizing current density is plotted as a function of anodizing time (Fig. 2d). The overpotential reduces markedly within the initial 30 min of anodizing, during which anodizing current density increases significantly. Thus, the OER active sites appear to be developed mainly during the current increase in anodizing at this anodizing temperature. The anodizing current is higher at ≥30°C, but the OER activity is reduced (Fig. 2a). Thus, there is no simple correlation between the anodizing current density and OER activity. After anodizing for 2 h at 20°C, the OER overpotential is as low as 0.245 mV.

In order to get insight into the anodizing temperature dependence of the OER activity, the anodized alloy was characterized after five OER cycles. The surface and cross-section of the alloy anodized at each temperature (Fig. 3) reveal that an anodic film of uniform thickness is formed at 30 and 40°C, whereas the locally thick non-uniform anodic film is developed at ≤20°C. In particular, the film thickness became >1 μm at thicker regions when the alloy was anodized at 15 and 20°C. At other anodizing temperatures, thin films of <350 nm are formed, although locally thick regions are present at 10°C. The thickness of the anodic film formed at 40°C is as low as 230 nm even though the anodizing current is the highest, being 50 mA cm^{-2}. A slightly thicker film is developed at 30°C, but the average thickness is as low as 340 nm. The thinner film formation at ≥30°C indicates the low efficiency of film formation, and the dissolution of alloy and gas evolution reactions occurred preferentially in anodizing at such relatively high temperatures. The films formed at ≥30°C contain no visible pores in the surface scanning electron micrographs, possibly because of the small pore size. Micro-cracks

are present in the anodic films, which can be seen from both surface and cross-section scanning electron micrographs. More obvious micro-cracks are developed at anodizing temperatures of 15 and 20°C, associated with the thicker film formation.

EDS analysis was conducted along with the surface SEM observations. As shown in Fig. 4a, the film composition is almost independent of the anodizing temperature. It was known that fluoride-rich anodic films were formed on this alloy in the present electrolyte [27]. However, Fig. 4a shows the formation of oxygen-rich films at all temperatures due to the conversion of fluoride-rich film to oxyhydroxide ones during CV cycles. The low fluorine content of <7 at% indicates the rather rapid conversion of fluoride to oxyhydroxide, which should be a primary reason for the immediate activation. Fig. 4b shows the composition of the alloy elements in the film. Compared with the substrate alloy composition, iron content is reduced, and nickel is enriched in the anodic films, suggesting a slightly preferential dissolution of iron during anodizing and subsequent OER. The iron concentration in the anodic films tends to be slightly reduced as the anodizing temperature increases at and above 15°C.

Raman spectra were also obtained after 5 CV cycles in the KOH electrolyte (Fig. 4c). The spectra obtained at all anodizing temperatures are similar, showing the highest peak at 550 cm^{-1}. This peak with a shoulder peak at 455 cm^{-1} is a characteristic peak of (NiFe)OOH [31]. The low wavenumber peak is stronger than the high wavenumber peak for the β-NiOOH, but the relative intensity of the lower wavenumber peak is reduced with an increase in the iron content [31]. The intensity ratio of the two peaks shown in Fig. 4c suggests that the iron-rich (NiFe)OOH is present in the anodic films after OER in agreement with the EDS analysis (Fig. 4b). An additional shoulder peak also appears at 683 cm^{-1} at all anodizing temperatures. This shoulder peak may be assigned to Fe_3O_4, which exhibits a most intense peak at ~680 cm^{-1} [32]. This phase may precipitate during OER after the dissolution of iron-containing species

in KOH electrolyte. It was reported that Fe_3O_4 did not reveal high OER activity [33], this phase may not contribute largely to the OER.

The surfaces of the anodized alloy after 5 CV cycles were analyzed by XPS (Fig. 5). XPS spectra (Fig. 5a-5e) reveal the presence of iron, nickel, cobalt, and oxygen, and the fluorine content appears low. The peak binding energies of Fe $2p_{3/2}$, Ni $2p_{3/2}$, and Co $2p_{3/2}$ are similar, regardless of anodizing temperature, corresponding to oxyhydroxides of these elements [34-36]. It was reported that Co^{3+} species exhibited almost no satellite peak in Co $2p_{3/2}$ spectra [37]. However, Co 2p spectra in Fig. 5 disclose a broad satellite peak at ~786 eV, suggesting the presence of Co^{2+} species in addition to Co^{3+} species. The O 1s spectra reveal two peaks at 530.0 eV and 531.5 eV, assigned to O^{2-}-type and OH-type oxygen species, respectively.

The composition of the surfaces was estimated using the peak areas of individual elements and plotted in Fig. 5f. It is obvious that fluoride concentration on the surface is less than 5 at% and the oxygen concentration is as high as 70 at%. The change in the ratio of alloying elements on the surface (Fig. 5g) indicates that the iron concentration decreases, whereas the nickel and cobalt concentrations increase with increased anodizing temperature. Preferential dissolution of iron appears to be promoted during anodizing of the alloy at higher temperatures. From XPS analysis, it can be confirmed that the FeNiCo oxyhydroxide is formed during OER in KOH electrolyte.

Fig. 6 shows the cross-section scanning electron micrographs of the alloy anodized at 20°C for different periods. A thin film of ~120 nm thickness is formed after anodizing for 400 s, with some thicker regions of ~400 nm thickness developing locally (Fig. 6a). The local thickening of the anodic film may be associated with the breakdown of the barrier layer, and the electric current concentration at the breakdown sites induces the local thickening of the anodic film. Such non-uniform film formation is known as the “local burning phenomenon” in anodizing aluminum in acid electrolytes and often occurs during galvanostatic anodizing at

high current densities [38, 39]. The non-uniform film thickening on the present alloy occurs within the anodizing time of 400 s, which is before the current minimum. The number density of the local thick regions increases at the anodizing time of 800 s (Fig. 6b), at which the anodizing current almost reaches the steady-state value. However, still thinner film regions of ~300 nm thickness remain on the surface and the coverage of the thicker film regions increases during anodizing at the steady-state current. The almost entire surface of the alloy is covered with thicker anodic film after anodizing for 1800 s (Fig. 6c), resulting in the high OER activity (Fig. 2d). The thicknesses of the anodic film after anodizing for 1800 s and 7200 s are similar, being 1.3 – 2.0 μm; no noticeable thickening of the anodic film occurs during prolonged anodizing at 20°C because of the dissolution of the anodic film.

High magnification scanning electron micrographs of cross-sections after anodizing for 400 s and 7200 s (Fig. 7) reveal the porous nature of the anodic films. Many spherical pores are seen in the anodic film formed after anodizing for 400 s. Even after anodizing for 7200 s, the pore morphology is not cylindrical, and a sponge-like porous film is a characteristic of the anodic films on this alloy, in contrast to the cylindrical pore formation in anodic alumina films in acid electrolytes.

We conducted EIS measurements to understand the high OER activity of the anodized alloy with a porous (FeNiCo)OOH film. The Nyquist plots of the alloy anodized at different temperatures are shown in Fig. 8a and 8b. Two semicircles are present, particularly obvious for the alloy anodized at 10°C. The semicircles are smaller for the OER active alloy anodized at 15 and 20°C compared to the alloy anodized at other temperatures, indicating the reduced charge transfer resistance for OER. The obtained spectra were fitted using an electrical equivalent circuit reported for oxide electrodes in alkaline media (Fig. 8c) [40]. R_s, R_f, and R_{ct} represent the electrolyte resistance, film resistance, and charge transfer resistance, respectively, in this equivalent circuit. The constant phase elements $(CPE)_1$ and $(CPE)_2$

represent the film and the double-layer capacitance, respectively. The constant phase element was introduced to account for the non-ideal capacitive behavior of the anodized alloy [41]. The CPE has the impedance in the form of

$$Z_{CPE} = 1/[Q(j\omega)^n]$$

where ω is the angular frequency and n is a non-dimensional number with a value of 0 < n < 1. The Q parameter is the magnitude of the CPE. In this study, the capacitance, C, was estimated from the following equation [41]:

$$C_i = Q_i^{1/n} R_i^{(1-n)/n} \ (i = f \ and \ ct \ or \ dl)$$

The fitted parameters are listed in Table 1, which shows that the OER active alloy electrodes anodized at 15 and 20°C exhibits low film and charge transfer resistance values and high double-layer capacitance. The high double-layer capacitance is likely related to the thicker film formation and high surface area. Table 2 shows the change in the fitted parameters with anodizing time. The charge transfer resistance is reduced, and the electric double-layer capacitance increases with anodizing time. Fig. 9a shows the changes in the charge transfer resistance and the double-layer capacitance with anodizing time to visualize these changes. The increase of the double-layer capacitance with anodizing time may be associated with the thickening of the anodic film. Since the charge transfer resistance is inverse proportional to the exchange current density, there is a similar anodizing time dependence between the charge transfer resistance and the overpotential (Fig. 2d). Fig. 9b shows the correlation between the electric double-layer capacitance and the OER current density at an overpotential of 270 mV. The double-layer capacitance obtained from cyclic voltammetry is also included in this plot. The OER activity appears to enhance with the electric double-layer capacitance, suggesting that the increment of the active sites by thickening of the porous anodic film is of primal importance in enhancing the OER activity of the anodized FeNiCo alloy. It was reported that NiOOH is conductive [42], and the Fe incorporation further enhances the conductivity [6].

Possibly because of the sufficient conductivity of the present (FeNiCo)OOH in the porous films, the thickening of the porous anodic films to >1 μm can effectively enhance the OER activity.

4. Conclusions

In this study, highly OER-active electrodes in an alkaline electrolyte were prepared by anodizing a commercial FeNiCo alloy in fluoride-containing ethylene glycol electrolyte at several temperatures. The sponge-like porous (FeNiCo)F_2 films formed by anodizing were converted immediately to an OER active (FeNiCo)OOH in KOH electrolyte. The anodizing temperature influenced the OER activity because of the change in the growth behavior of the porous anodic films. Only thin films of <350 nm were formed at ≥30°C even though the anodizing current density was high, resulting in the low OER activity. When anodizing was conducted at ≤20°C, film growth proceeded nonuniformly, possibly because of the local breakdown of the barrier layer. The OER activity increased as the thicker film regions expanded to the entire surface, and a good correlation was found between the electric double-layer capacitance and OER activity.

Declaration of Competing Interest

The authors declare no conflict of interest.

Acknowledgments

This work was supported in part by JSPS KAKENHI grant no. 19H02469 and the University Research Aid from the JFE 21st Century Foundation. A part of this work was conducted at the Promotion Office for the Nanotechnology Collaboration and Laboratory of XPS analysis, Hokkaido University, supported by the “Nanotechnology Platform” Program of the Ministry

of Education, Culture, Sports, Science and Technology (MEXT), Japan.

References

[1] O. Schmidt, A. Gambhir, I. Staffell, A. Hawkes, J. Nelson, S. Few, Future cost and performance of water electrolysis: An expert elicitation study, Int. J. Hydrogen Energy, 42 (2017) 30470-30492. 10.1016/j.ijhydene.2017.10.045.

[2] A. Buttler, H. Spliethoff, Current status of water electrolysis for energy storage, grid balancing and sector coupling via power-to-gas and power-to-liquids: A review, Renewable and Sustainable Energy Reviews, 82 (2018) 2440-2454. https://doi.org/10.1016/j.rser.2017.09.003.

[3] D.A. Corrigan, The catalysis of the oxygen evolution reaction by iron impurities in thin film nickel oxide electrodes, J. Electrochem. Soc., 134 (1987) 377-384. 10.1149/1.2100463.

[4] J. Landon, E. Demeter, N. Inoglu, C. Keturakis, I.E. Wachs, R. Vasic, A.I. Frenkel, J.R. Kitchin, Spectroscopic characterization of mixed fe-ni oxide electrocatalysts for the oxygen evolution reaction in alkaline electrolytes, ACS Catalysis, 2 (2012) 1793-1801. 10.1021/cs3002644.

[5] M. Gong, Y. Li, H. Wang, Y. Liang, J.Z. Wu, J. Zhou, J. Wang, T. Regier, F. Wei, H. Dai, An advanced Ni-Fe layered double hydroxide electrocatalyst for water oxidation, J. Am. Chem. Soc., 135 (2013) 8452-8455. 10.1021/ja4027715.

[6] L. Trotochaud, S.L. Young, J.K. Ranney, S.W. Boettcher, Nickel-iron

oxyhydroxide oxygen-evolution electrocatalysts: The role of intentional and incidental iron incorporation, J. Am. Chem. Soc., 136 (2014) 6744-6753. 10.1021/ja502379c.

[7] Y.Y. Feng, H.J. Zhang, Y. Zhang, X. Li, Y. Wang, Ultrathin two-dimensional free-standing sandwiched NiFe/C for high-efficiency oxygen evolution reaction, ACS Appl. Mater. Interfaces, 7 (2015) 9203-9210. 10.1021/acsami.5b01467.

[8] X. Lu, C. Zhao, Electrodeposition of hierarchically structured three-dimensional nickel-iron electrodes for efficient oxygen evolution at high current densities, Nat. Commun., 6 (2015) 6616. 10.1038/ncomms7616.

[9] D.F. Abbott, E. Fabbri, M. Borlaf, F. Bozza, R. Schäublin, M. Nachtegaal, T. Graule, T.J. Schmidt, Operando X-ray absorption investigations into the role of Fe in the electrochemical stability and oxygen evolution activity of $Ni_{1-x}Fe_xO_y$ nanoparticles, Journal of Materials Chemistry A, 6 (2018) 24534-24549. 10.1039/c8ta09336a.

[10] C. Pei, Y. Gu, Z. Liu, X. Yu, L. Feng, Fluoridated iron-nickel layered double hydroxide for enhanced performance in the oxygen evolution reaction, ChemSusChem, 12 (2019) 3849-3855. 10.1002/cssc.201901153.

[11] Y. Zhou, N. López, The role of Fe species on NiOOH in oxygen evolution reactions, ACS Catalysis, 10 (2020) 6254-6261. 10.1021/acscatal.0c00304.

[12] F. Dionigi, Z. Zeng, I. Sinev, T. Merzdorf, S. Deshpande, M.B. Lopez, S. Kunze, I. Zegkinoglou, H. Sarodnik, D. Fan, A. Bergmann, J. Drnec, J.F. Araujo, M. Gliech, D. Teschner, J. Zhu, W.X. Li, J. Greeley, B.R. Cuenya, P. Strasser, In-situ structure and catalytic mechanism of NiFe and CoFe layered double hydroxides during oxygen evolution, Nat. Commun., 11 (2020) 2522. 10.1038/s41467-020-16237-1.

[13] H. Sun, Z. Yan, F. Liu, W. Xu, F. Cheng, J. Chen, Self-supported transition-metal-based electrocatalysts for hydrogen and oxygen evolution, Adv Mater, 32 (2020) e1806326. 10.1002/adma.201806326.

[14] K. Shahzad, D. Kowalski, C. Zhu, Y. Aoki, H. Habazaki, Ex situ evidence for the role of a fluoride-rich layer switching the growth of nanopores to nanotubes: A missing piece of the anodizing puzzle, ChemElectroChem, 5 (2018) 610-618. 10.1002/celc.201701103.

[15] K. Shahzad, E. Tsuji, Y. Aoki, S. Nagata, H. Habazaki, Formation and field-assisted dissolution of anodic films on iron in fluoride-containing organic electrolyte, Electrochim. Acta, 151 (2015) 363-369. 10.1016/j.electacta.2014.10.132.

[16] Y. Konno, E. Tsuji, P. Skeldon, G.E. Thompson, H. Habazaki, Factors influencing the growth behaviour of nanoporous anodic films on iron under

galvanostatic anodizing, J. Solid State Electrochem., (2012) 1-10. 10.1007/s10008-012-1833-1.

[17] H. Habazaki, Y. Konno, Y. Aoki, P. Skeldon, G.E. Thompson, Galvanostatic growth of nanoporous anodic films on iron in ammonium fluoride-ethylene glycol electrolytes with different water contents, J. Phys. Chem. C, 114 (2010) 18853-18859. Doi 10.1021/Jp1078136.

[18] C.Y. Lee, Z.X. Su, K. Lee, H. Tsuchiya, P. Schmuki, Self-organized cobalt fluoride nanochannel layers used as a pseudocapacitor material, Chem. Commun., 50 (2014) 7067-7070. 10.1039/c4cc01195c.

[19] J.S. Kang, J. Kim, J.S. Kim, K. Nam, H. Jo, Y.J. Son, J. Kang, J. Jeong, H. Choe, T.-H. Kwon, Y.-E. Sung, Electrochemically synthesized mesoscopic nickel oxide films as photocathodes for dye-sensitized solar cells, ACS Applied Energy Materials, 1 (2018) 4178-4185. 10.1021/acsaem.8b00834.

[20] L. Wang, G. Zhang, Y. Liu, W. Li, W. Lu, H. Huang, Facile synthesis of a mechanically robust and highly porous nio film with excellent electrocatalytic activity towards methanol oxidation, Nanoscale, 8 (2016) 11256-11263. 10.1039/c6nr01991a.

[21] M. Chiku, M. Toda, E. Higuchi, H. Inoue, NiO layers grown on a Ni substrate by galvanostatic anodization as a positive electrode material for aqueous hybrid

capacitors, J. Power Sources, 286 (2015) 193-196. 10.1016/j.jpowsour.2015.03.095.

[22] Y.J. Son, K. Kawashima, B.R. Wygant, C.H. Lam, J.N. Burrow, H. Celio, A. Dolocan, J.G. Ekerdt, C.B. Mullins, Anodized nickel foam for oxygen evolution reaction in Fe-free and unpurified alkaline electrolytes at high current densities, ACS Nano, (2021). 10.1021/acsnano.0c10788.

[23] H. Schäfer, D.M. Chevrier, P. Zhang, J. Stangl, K. Müller-Buschbaum, J.D. Hardege, K. Kuepper, J. Wollschläger, U. Krupp, S. Dühnen, M. Steinhart, L. Walder, S. Sadaf, M. Schmidt, Electro-oxidation of Ni42 steel: A highly active bifunctional electrocatalyst, Adv. Func. Mater., 26 (2016) 6402-6417. 10.1002/adfm.201601581.

[24] J. Fan, Z. Chen, H. Shi, G. Zhao, In situ grown, self-supported iron-cobalt-nickel alloy amorphous oxide nanosheets with low overpotential toward water oxidation, Chem Commun (Camb), 52 (2016) 4290-4293. 10.1039/c5cc09699e.

[25] X. Fan, Y. Liu, S. Chen, J. Shi, J. Wang, A. Fan, W. Zan, S. Li, W.A. Goddard, 3rd, X.M. Zhang, Defect-enriched iron fluoride-oxide nanoporous thin films bifunctional catalyst for water splitting, Nat Commun, 9 (2018) 1809. 10.1038/s41467-018-04248-y.

[26] N. Yamada, S. Kitano, Y. Yato, D. Kowalski, Y. Aoki, H. Habazaki, In situ

activation of anodized Ni–Fe alloys for the oxygen evolution reaction in alkaline media, ACS Applied Energy Materials, 3 (2020) 12316-12326. 10.1021/acsaem.0c02362.

[27] M. Nishimoto, S. Kitano, D. Kowalski, Y. Aoki, H. Habazaki, Highly active and durable FeNiCo oxyhydroxide oxygen evolution reaction electrocatalysts derived from fluoride precursors, ACS Sustainable Chemistry & Engineering, 9 (2021) 9465-9473. 10.1021/acssuschemeng.1c03116.

[28] A. Lasia, A. Rami, Kinetics of hydrogen evolution on nickel electrodes, Journal of Electroanalytical Chemistry and Interfacial Electrochemistry, 294 (1990) 123-141. https://doi.org/10.1016/0022-0728(90)87140-F.

[29] W. Lee, S.J. Park, Porous anodic aluminum oxide: Anodization and templated synthesis of functional nanostructures, Chem Rev, 114 (2014) 7487-7556. 10.1021/cr500002z.

[30] F. Li, L. Zhang, R.M. Metzger, On the growth of highly ordered pores in anodized aluminum oxide, Chem. Mater., 10 (1998) 2470-2480. 10.1021/cm980163a.

[31] M.W. Louie, A.T. Bell, An investigation of thin-film Ni-Fe oxide catalysts for the electrochemical evolution of oxygen, J Am Chem Soc, 135 (2013) 12329-12337. 10.1021/ja405351s.

[32] D.L.A. de Faria, S. Venâncio Silva, M.T. de Oliveira, Raman microspectroscopy of some iron oxides and oxyhydroxides, J. Raman Spectrosc., 28 (1997) 873-878. https://doi.org/10.1002/(SICI)1097-4555(199711)28:11<873::AID-JRS177>3.0.CO;2-B.

[33] Y. Luo, H. Yang, P. Ma, S. Luo, Z. Zhao, J. Ma, Fe_3O_4/CoO interfacial nanostructure supported on carbon nanotubes as a highly efficient electrocatalyst for oxygen evolution reaction, ACS Sustainable Chemistry & Engineering, 8 (2020) 3336-3346. 10.1021/acssuschemeng.9b07292.

[34] J. Fester, A. Walton, Z. Li, J.V. Lauritsen, Gold-supported two-dimensional cobalt oxyhydroxide (CoOOH) and multilayer cobalt oxide islands, Phys Chem Chem Phys, 19 (2017) 2425-2433. 10.1039/c6cp07901f.

[35] A.N. Mansour, C.A. Melendres, Characterization of electrochemically prepared γ-NiOOH by XPS, Surface Science Spectra, 3 (1994) 271-278. 10.1116/1.1247756.

[36] K. Asami, K. Hashimoto, The X-ray photo-electron spectra of several oxides of iron and chromium, Corros. Sci., 17 (1977) 559-570. https://doi.org/10.1016/S0010-938X(77)80002-4.

[37] D. Barreca, A. Gasparotto, O.I. Lebedev, C. Maccato, A. Pozza, E. Tondello, S. Turner, G. Van Tendeloo, Controlled vapor-phase synthesis of cobalt oxide

nanomaterials with tuned composition and spatial organization, CrystEngComm, 12 (2010) 2185-2197. 10.1039/B926368N.

[38] T. Aerts, I. De Graeve, H. Terryn, Study of initiation and development of local burning phenomena during anodizing of aluminium under controlled convection, Electrochim. Acta, 54 (2008) 270-279. 10.1016/j.electacta.2008.08.004.

[39] B. Gastón-García, E. García-Lecina, J.A. Díez, M. Belenguer, C. Müller, Local burning phenomena in sulfuric acid anodizing: Analysis of porous anodic alumina layers on AA1050, Electrochem. Solid-State Letters, 13 (2010) C33. 10.1149/1.3478482.

[40] S. Palmas, F. Ferrara, A. Vacca, M. Mascia, A.M. Polcaro, Behavior of cobalt oxide electrodes during oxidative processes in alkaline medium, Electrochim. Acta, 53 (2007) 400-406. 10.1016/j.electacta.2007.01.085.

[41] B. Hirschorn, M.E. Orazem, B. Tribollet, V. Vivier, I. Frateur, M. Musiani, Determination of effective capacitance and film thickness from constant-phase-element parameters, Electrochim. Acta, 55 (2010) 6218-6227. http://dx.doi.org/10.1016/j.electacta.2009.10.065.

[42] M.J. Natan, D. Belanger, M.K. Carpenter, M.S. Wrighton, pH-sensitive nickel(II) hydroxide-based microelectrochemical transistors, J Phys. Chem., 91

(1987) 1834-1842. 10.1021/j100291a031.

Table 1 Fitted EIS parameters for the FeNiCo alloy anodized at 10 V and several electrolyte temperatures, followed by five OER cycles in 1.0 mol dm^{-3} KOH electrolyte.

Anodizing temperature (°C)	R_f (Ω cm^2)	C_f (mF cm^{-2})	R_{ct} (Ω cm^2)	C_{dl} (F cm^{-2})
10	3.31	3.14×10^{-4}	4.33	28.8
15	0.589	1.82×10^{-2}	1.45	89.8
20	0.335	7.05×10^{-2}	1.22	150
30	1.02	1.14	6.31	24.3
40	1.80	16.7	7.89	21.0

Table 2 Fitted EIS parameters for the FeNiCo alloy anodized at 10 V for different periods, followed by five OER cycles in 1.0 mol dm^{-3} KOH electrolyte.

Anodizing time (s)	R_f (Ω cm^2)	C_f (mF cm^{-2})	R_{ct} (Ω cm^2)	C_{dl} (F cm^{-2})
200	0.303	5.88	3.05	12.9
300	0.227	22.7	2.98	14.7
400	0.237	13.3	2.41	16.9
800	0.696	40.8	1.8	53.5
1000	0.253	83.9	1.23	112
1800	0.158	56.1	0.949	154
3600	0.477	62.0	0.757	226
7200	0.138	60.0	0.851	207

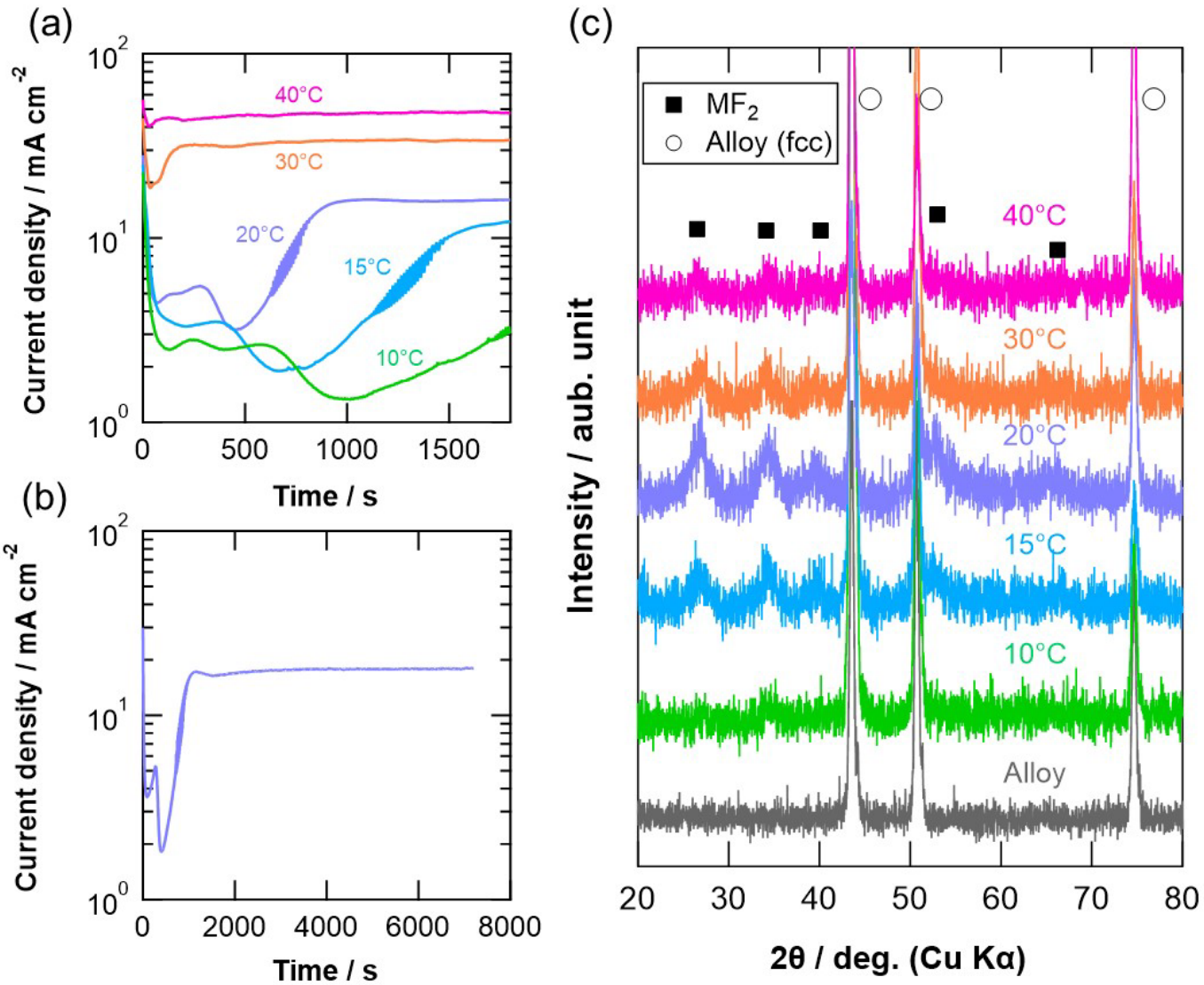

Fig. 1 (a) Current transients of the FeNiCo alloy during anodizing at 10 V in ethylene glycol electrolyte containing 0.54 mol dm^{-3} NH_4F and 2.5 mol dm^{-3} H_2O at several temperatures for 1800 s, (b) current transient during prolonged anodizing at 20° C, (c) XRD patterns of the alloy as-received and anodized at several temperatures for 1800 s.

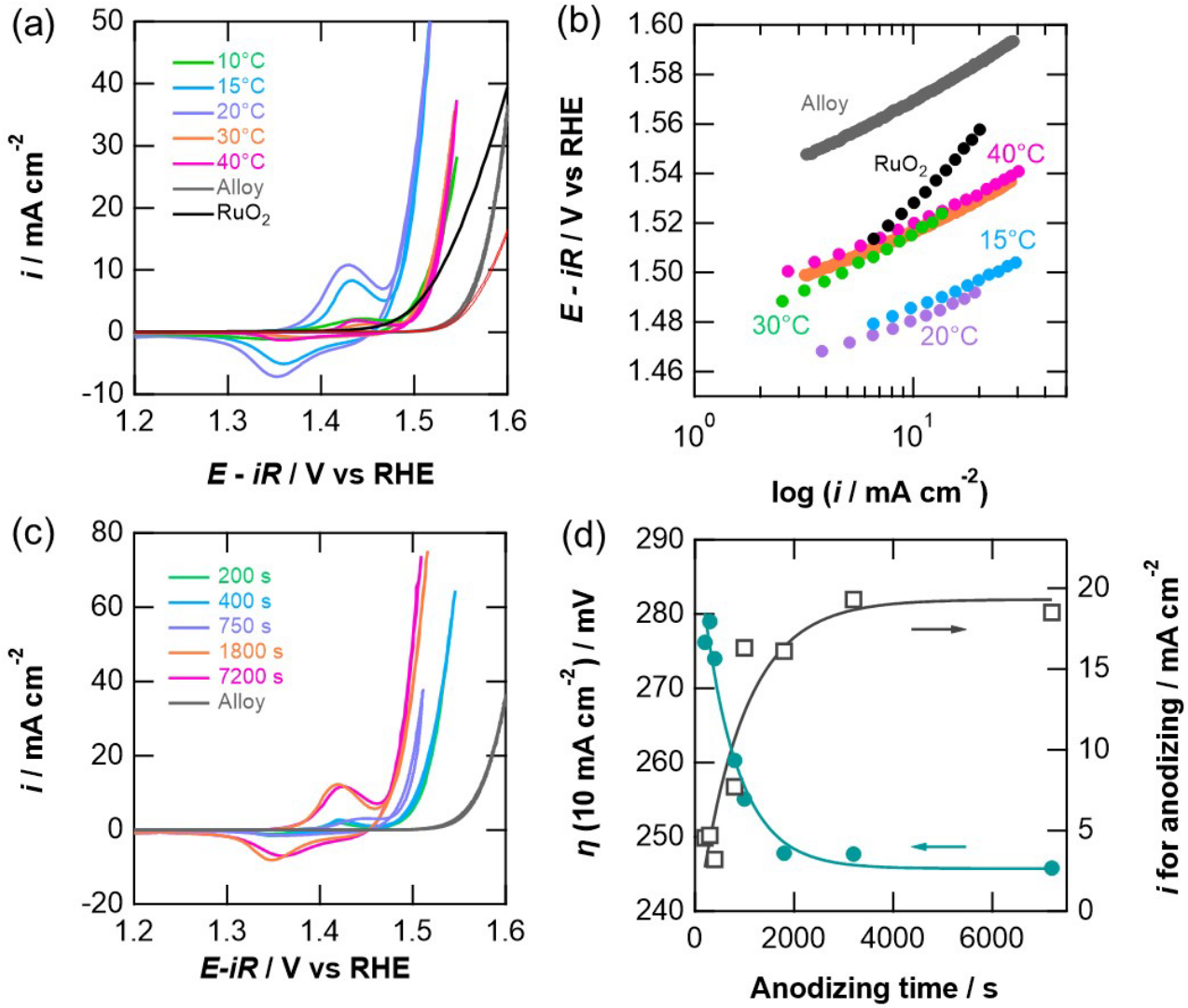

Fig. 2 (a) CV curves and (b) Tafel plots for OER of the alloy as-received and anodized at 10 V in ethylene glycol electrolyte containing 0.54 mol dm^{-3} NH_4F and 2.5 mol dm^{-3} H_2O at several temperatures for 1800 s and RuO_2, measured in 1.0 mol dm^{-3} KOH electrolyte, (c) CV curves for OER of the alloy anodized at 20° C for different periods, and (d) changes in the OER overpotential at 10 mA cm^{-2} and anodizing current density with anodizing time.

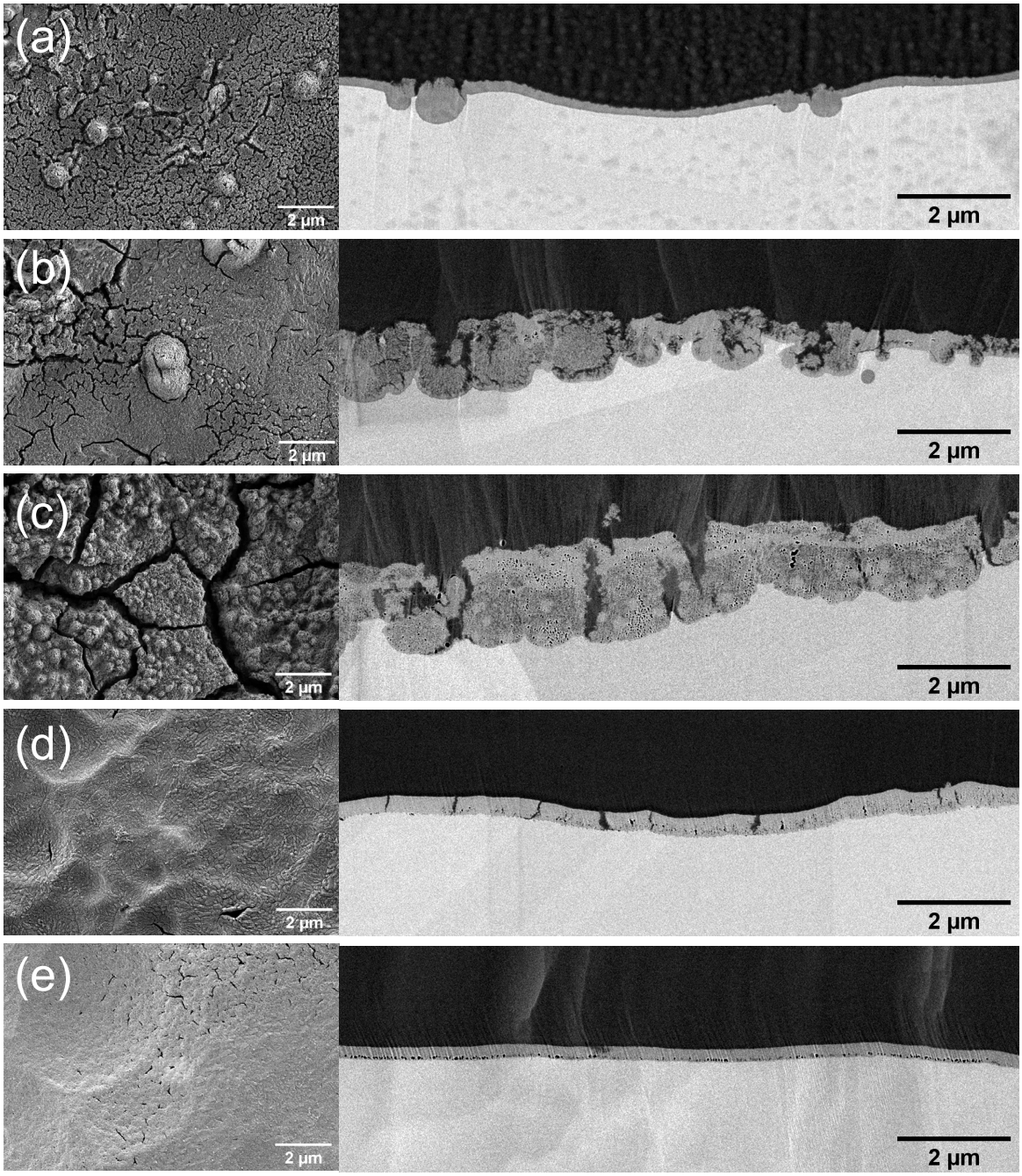

Fig. 3 Surface and cross-section scanning electron micrographs of the FeNiCo alloy anodized at 10 V in ethylene glycol electrolyte containing 0.54 mol dm^{-3} NH_4F and 2.5 mol dm^{-3} H_2O at (a) 10° C, (b) 15° C, (c) 20° C, (d) 30° C, and (e) 40° C for 1800 s, followed by five OER CV cycles in 1.0 mol dm^{-3} KOH electrolyte.

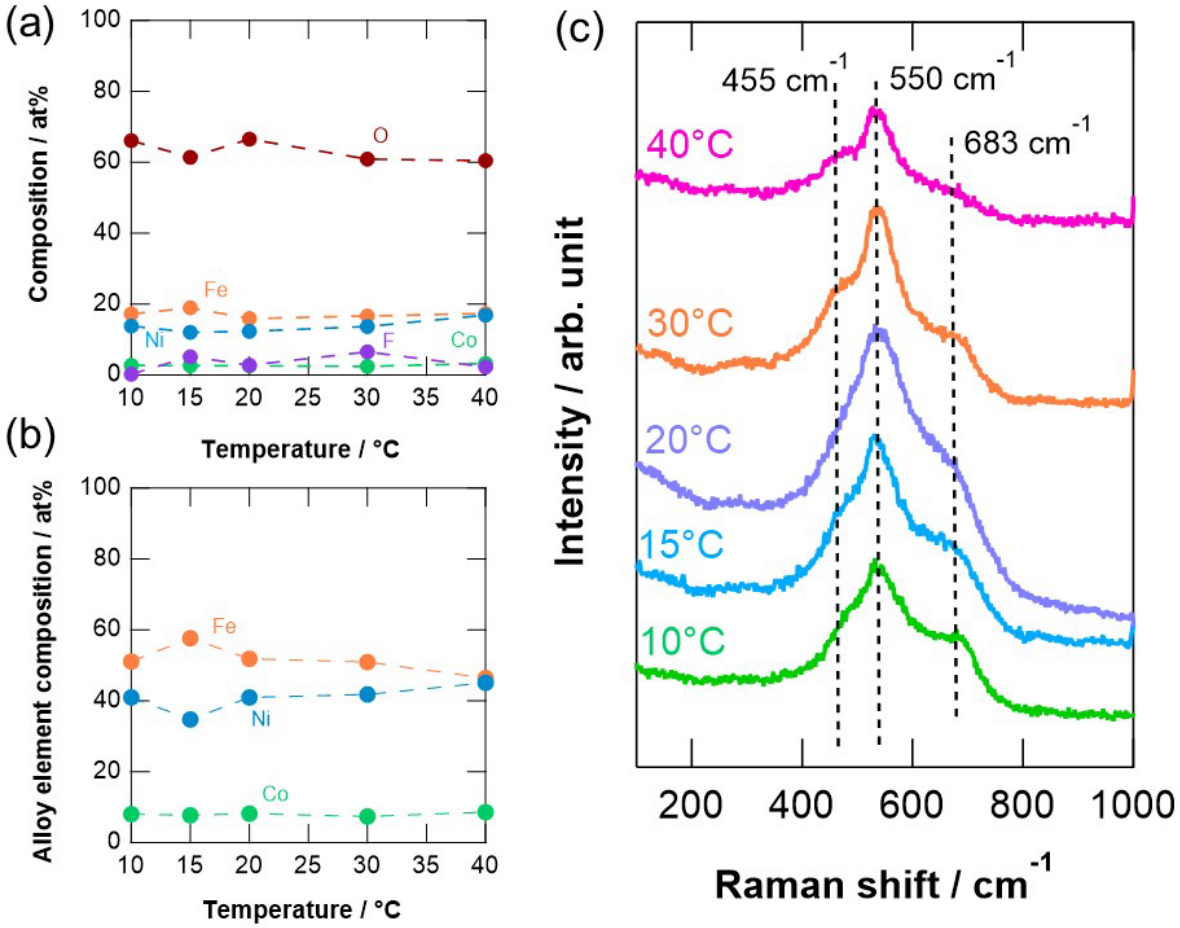

Fig. 4 (a, b) The anodic film compositions and (c) of the anodic films on the FeNiCo alloy anodized at 10 V in ethylene glycol electrolyte containing 0.54 mol dm^{-3} NH_4F and 2.5 mol dm^{-3} H_2O at several temperatures for 1800 s, followed by five OER CV cycles in 1.0 mol dm^{-3} KOH electrolyte.

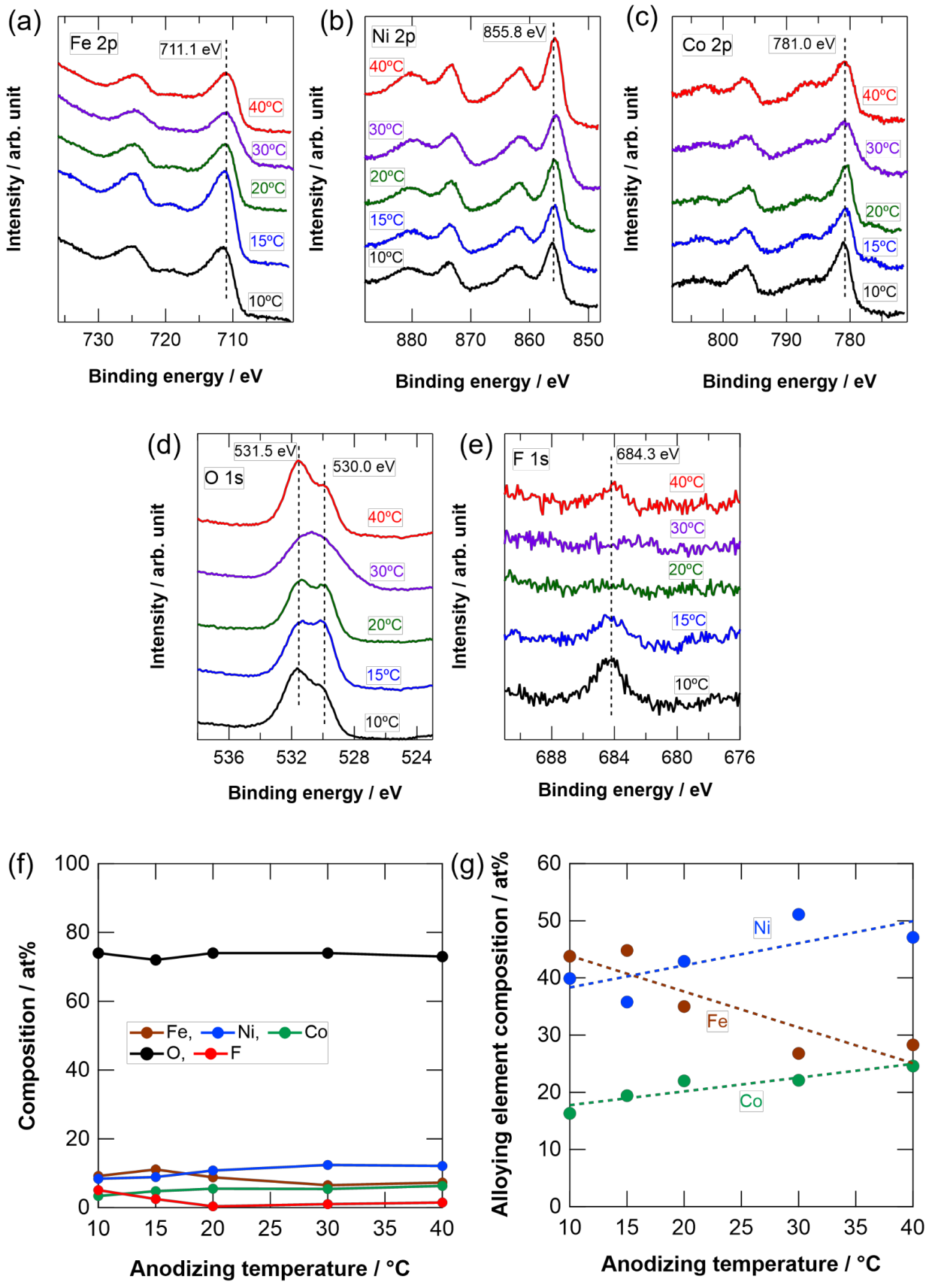

Fig. 5 (a) Fe 2p, (b) Ni 2p, (c) Co 2p, (d) O 1s, (e) F 1s XPS spectra, and (f-g) surface composition of the FeNiCo alloy anodized at 10 V in ethylene glycol electrolyte containing 0.54 mol dm^{-3} NH_4F and 2.5 mol dm^{-3} H_2O at several temperatures for 1800 s, followed by five OER CV cycles in 1.0 mol dm^{-3} KOH electrolyte.

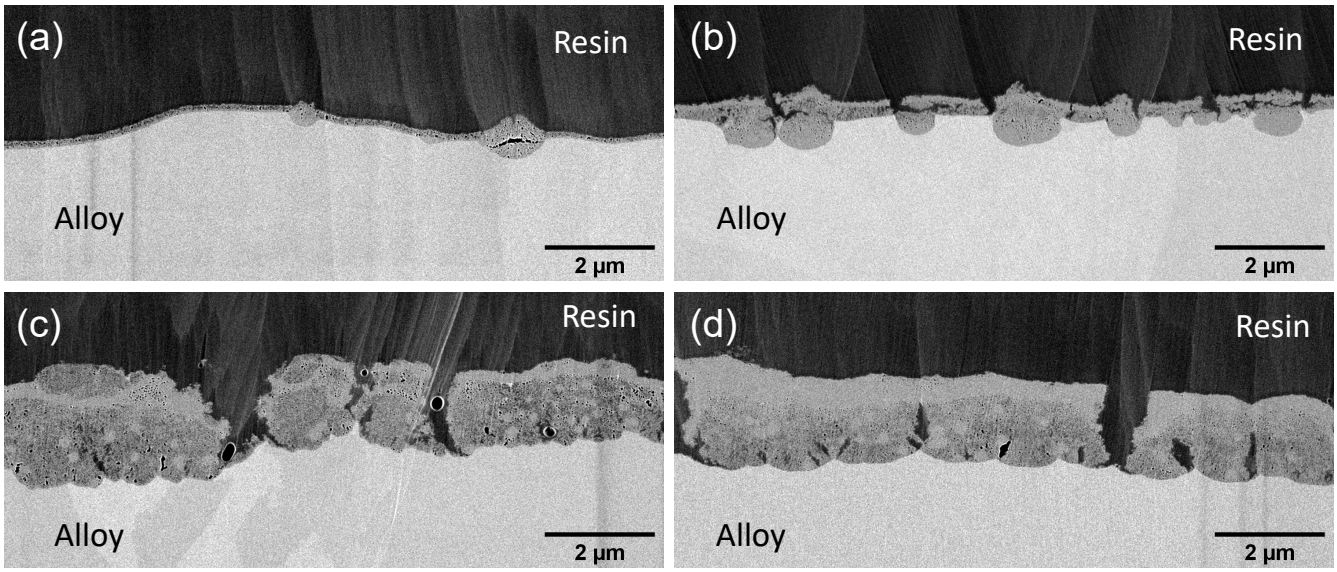

Fig. 6 Cross-section scanning electron micrographs of the FeNiCo alloy anodized at 10 V in ethylene glycol electrolyte containing 0.54 mol dm^{-3} NH_4F and 2.5 mol dm^{-3} H_2O at 20° C for (a) 400 s, (b) 800 s, (c) 1800 s and (d) 7200 s, followed by five OER CV cycles in 1.0 mol dm^{-3} KOH electrolyte.

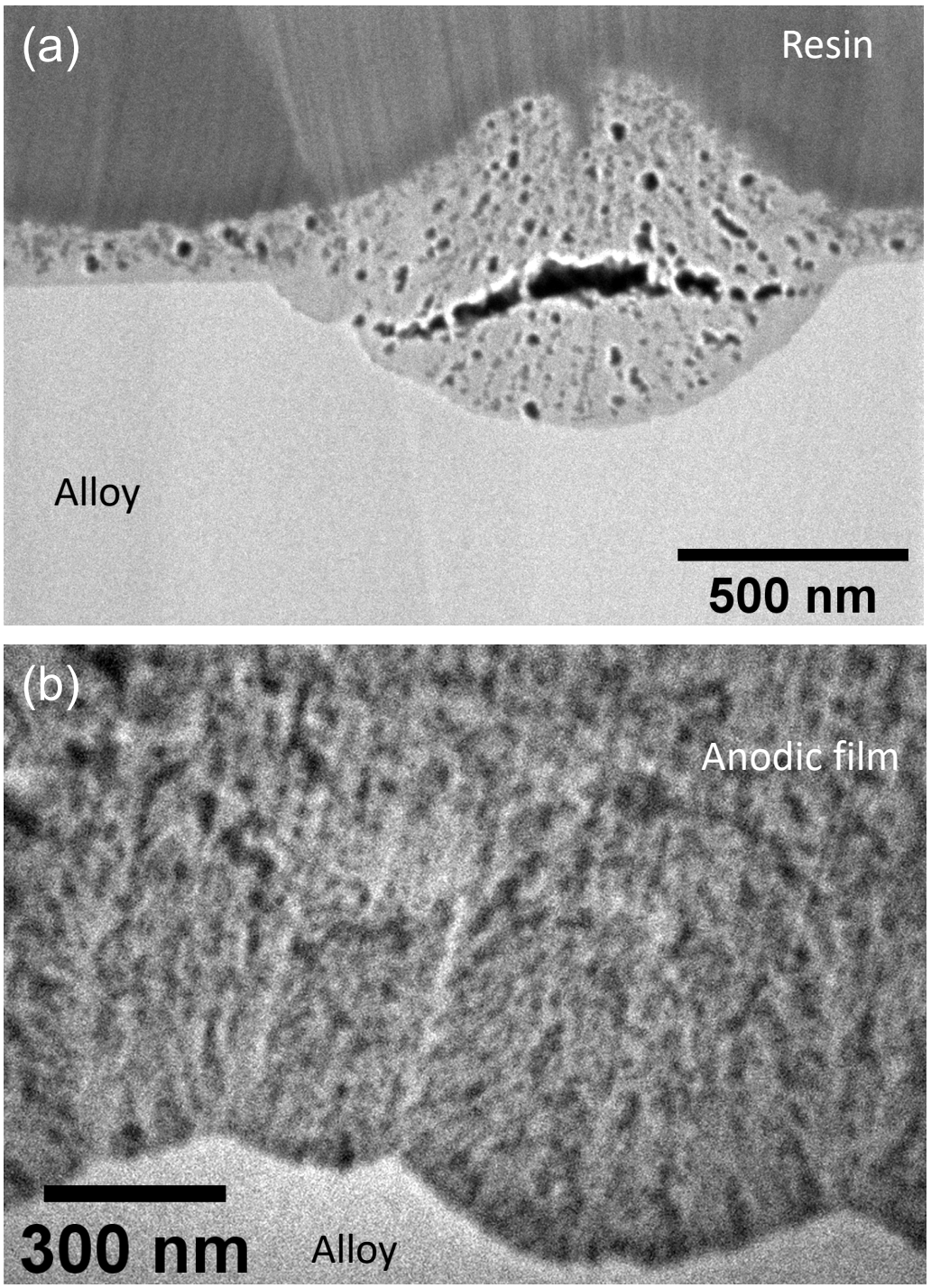

Fig. 7 High magnification cross-section scanning electron micrographs of the FeNiCo alloy anodized at 10 V in ethylene glycol electrolyte containing 0.54 mol dm^{-3} NH_4F and 2.5 mol dm^{-3} H_2O at 20° C for (a) 400 s and (b) 7200 s, followed by five OER CV cycles in 1.0 mol dm^{-3} KOH electrolyte.

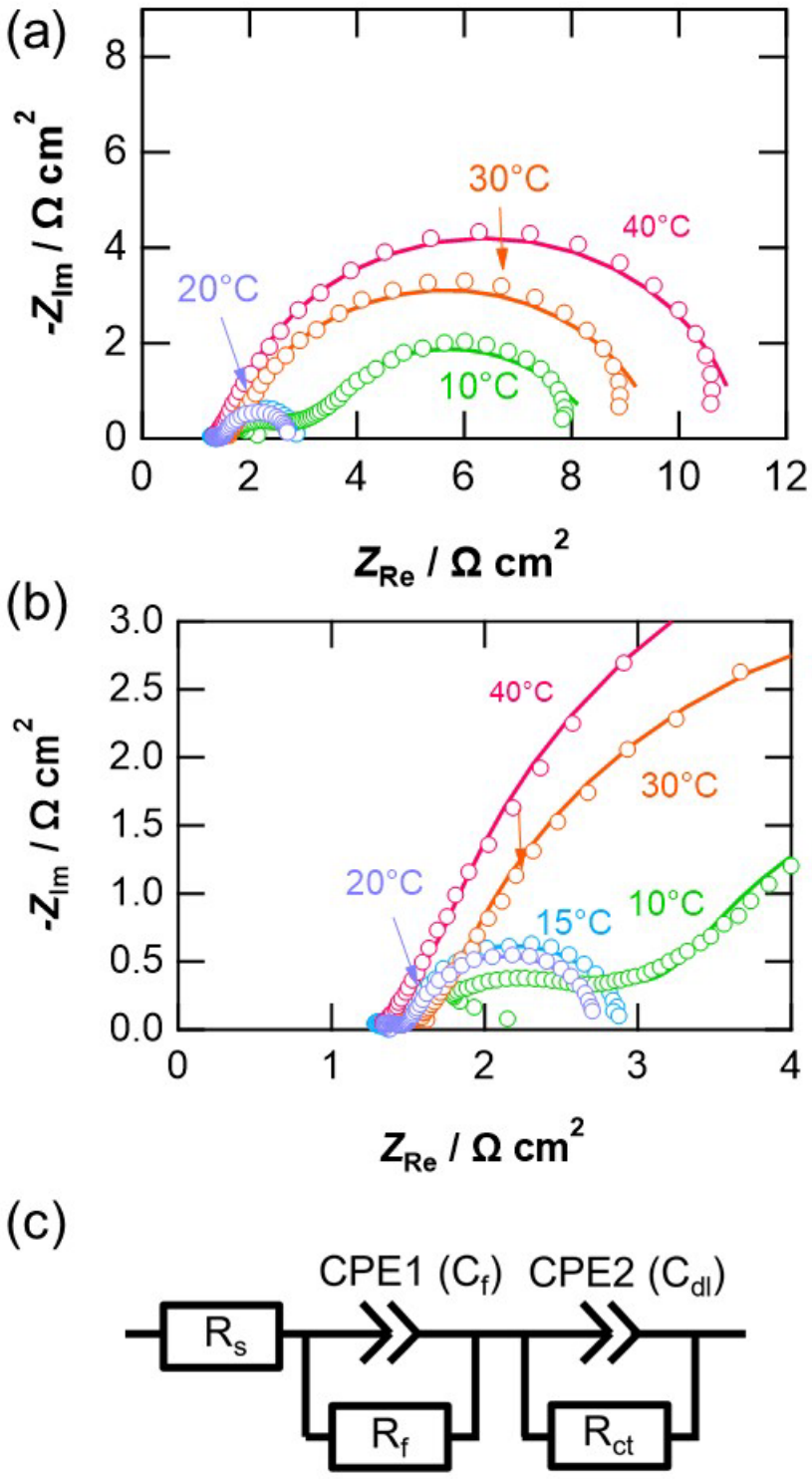

Fig. 8 (a, b) EIS Niquist plots of the FeNiCo alloy anodized at 10 V in ethylene glycol electrolyte containing 0.54 mol dm^{-3} NH_4F and 2.5 mol dm^{-3} H_2O at several temperatures for 1800 s, followed by five OER CV cycles in 1.0 mol dm^{-3} KOH electrolyte and (c) an equivalent electric circuit used to fit the EIS spectra.

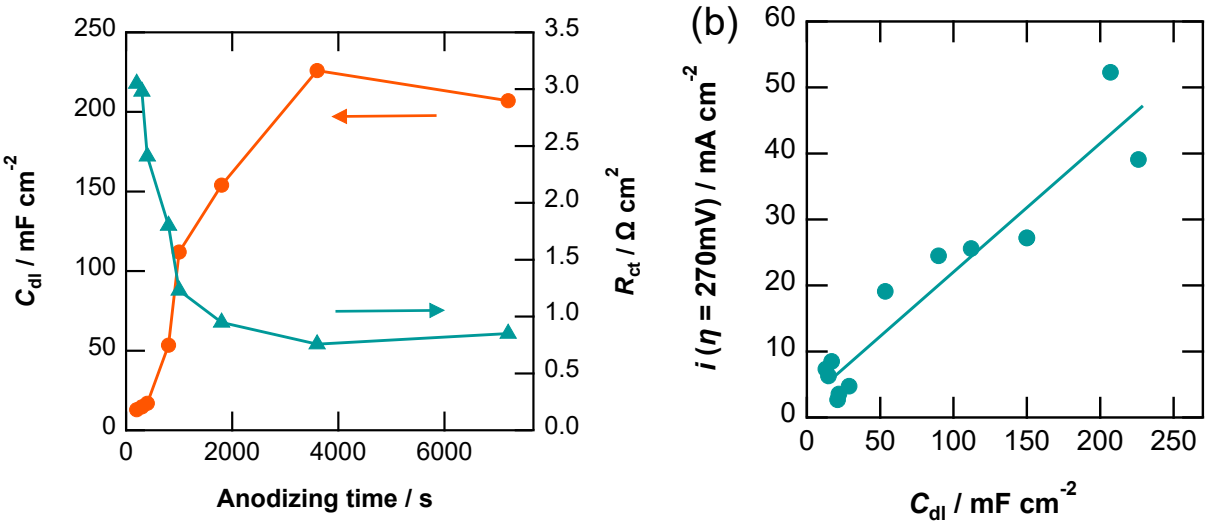

Fig. 9 (a) Changes in the charge transfer resistance and the electric double-layer capacitance with anodizing time and (b) the correlation between the OER current density at an overpotential of 270 mV and the electric double-layer capacitance.